ACS APPLIED MATERIALS & INTERFACES

Research Article

www.acsami.org

Modeling the Optical Properties of Bowtie Antenna Generated By Self-Assembled Ag Triangular Nanoprisms

David A. Rosen and Andrea R. Tao*

NanoEngineering Department, University of California, San Diego, 9500 Gilman Drive MC 0448, La Jolla, California 92093-0448, United States

ABSTRACT: Self-organized metal nanoparticles often possess assembly defects that can have a profound impact on the optical properties of the resulting nanoparticle assembly. Modeling these defects and evaluating their optical outcomes can provide a better understanding of how to design the assembly process and can evaluate the quality of the resulting materials. Here, we use finite element methods to examine the fabrication of bowtie nanoantenna, a commonly sought-after plasmonic structure with resonances in the visible and near-infrared wavelengths, through the self-assembly of colloidal triangular Ag nanoprisms. We model perfect and defective antenna structures and examine the effects of commonly observed assembly defects such as imperfect nanoprism shapes, off-axis antenna structures, and trimer or tetramer formation. We also evaluate the ability to fabricate antenna structures that possess comparable structural parameters (e.g., thickness, gap distance) to top-down lithographic techniques. We find that structural defects in self-assembled bowties can shift the resonant wavelength of the antenna by as much as 200 nm. Our models also indicate that self-assembled bowties possess high defect tolerances with respect to near-field enhancement, suggesting that they are viable structures for nanophotonic and nanoplasmonic applications.

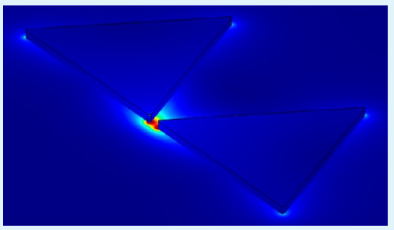

KEYWORDS: *Surface plasmon, finite element method, LSPR, field enhancement, bowtie, antenna*

INTRODUCTION

Metal nanostructures composed of Au and Ag behave like optical antennae by supporting the excitation of localized surface plasmon resonances (LSPRs), where conduction electrons of the metal oscillate in resonance with incident light to produce intense electromagnetic fields localized at the metal surface. Metal nanostructure size, shape, and arrangement are critical in determining the LSPR wavelength and the magnitude of the resulting field enhancement. Hot spots, where the electromagnetic field is highly confined within a small volume, are particularly pronounced at sharp nanoscale features (i.e., the antenna effect) and small gaps between adjacent metal surfaces. Recent work has focused on tailoring hot spot properties by thoughtfully designing metal nanostructures with anisotropic geometries such as bowtie antennas,[1] nanoholes,[2,3] triangle arrays formed by nanosphere lithography,[4,5] and nanocrescents.[6,7] These geometries can be produced using top-down approaches such as e-beam lithography, as in the case of bowties, or by using template-directed deposition of metal such as nanosphere lithography.

In contrast to these fabrication techniques, self-assembly approaches are advantageous because they can be carried out on a massively parallel scale to generate complex architectures using metal nanocrystal building blocks. Colloidal metal nanocrystals can be synthesized in large batches by wet chemical synthesis and typically possess crystallographically defined facets, edges, and corners that enable geometry-specific coordination. We recently demonstrated that plasmonic hot spots can be fabricated using a bottom-up approach by assembling Ag nanocubes, Au nanorods, and Ag triangular nanoprisms into oriented nanojunctions.[8,9] In this method, shaped Ag or Au nanocrystals are grafted with polymer chains of varying length and chemistry and then embedded within a bulk polymer matrix. Spontaneous phase segregation between polymer and nanocrystal components causes the nanocrystals to assemble into oriented dimers and one-dimensional strings. Hot spots are generated in the nanojunctions (i.e., the gap between nanocrystals) produced by these assemblies.

Using the polymer-directed assembly described above, bowtie structures can be fabricated by assembling colloidal triangular Ag nanoprisms. Bowtie antennas are particularly intriguing plasmonic structures because they are highly polarizable and produce large near-field enhancements within their nanojunction gap. Bowtie structures, or variations of bowtie structures such as inverse bowties,[10] have been used to produce large field enhancements for surface-enhanced Raman spectroscopy,[11] photocatalysis,[12] plasmonic lasers,[13] and single-molecule fluorescence.[14] To assemble bowties, Ag triangular nanoprisms are first synthesized using an aqueous seed-mediated growth method at room temperature. Figure 1a shows a typical extinction spectrum for a dispersion of Ag nanoprisms in water, taken by UV−visible spectroscopy. In agreement with previous reports,[15] the spectrum displays peaks for the in-plane dipolar LSPR mode at λ = 699 nm, the in-plane quadrupolar LSPR mode at λ = 490 nm, and the out-of-plane quadrupolar mode at λ = 337 nm. Depending on the reaction

Received: December 13, 2013
Accepted: February 17, 2014
Published: February 17, 2014

   dx.doi.org/10.1021/am4057612 | ACS Appl. Mater. Interfaces 2014, 6, 4134−4142

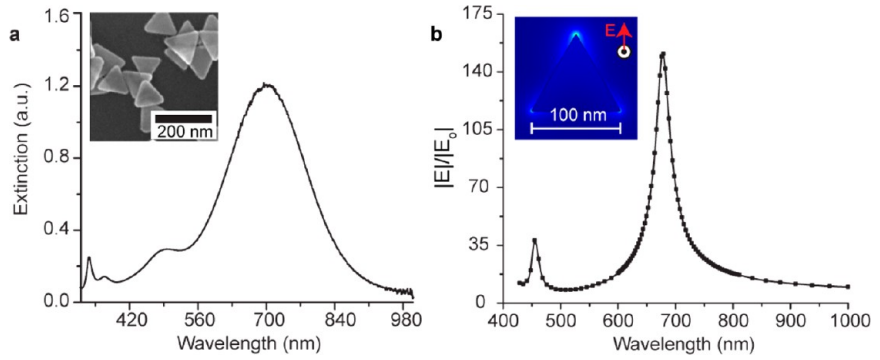

Figure 1. (a) UV−vis extinction spectra of colloidal Ag nanoprisms. Inset shows a SEM image of unassembled nanoprisms. (b) Simulated electric field enhancement ($|E|/|E_o|$) spectra of a single Ag nanoprism. Inset shows the areas of high electric field present at the resonance wavelength of λ = 679 nm.

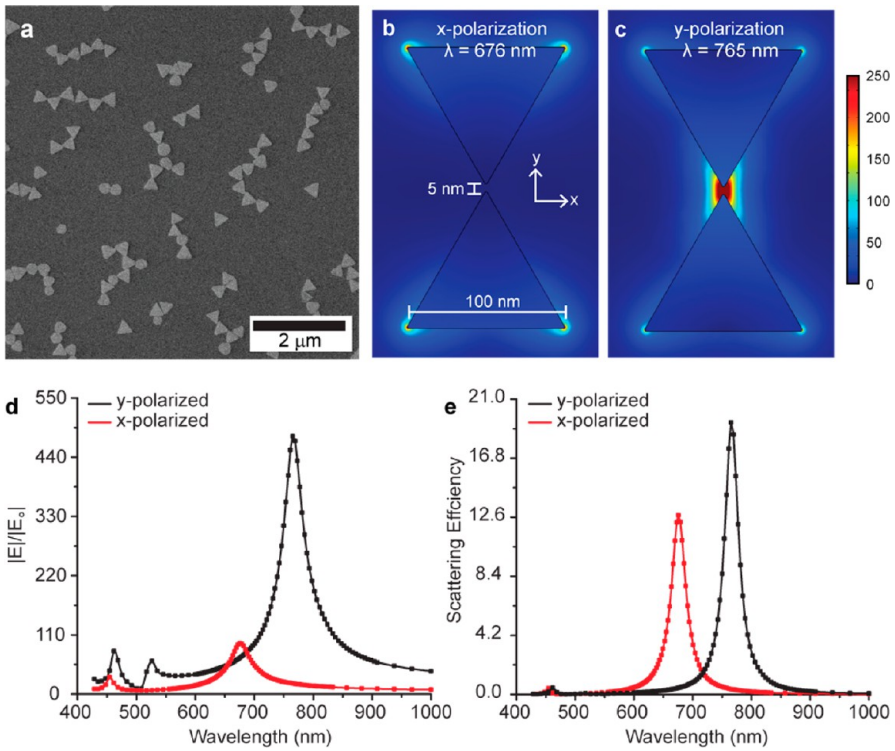

Figure 2. (a) SEM image of self-assembled colloidal nanoprisms into bowtie structures. (b,c) Simulated near-field intensities for the perfectly assembled bowtie structure taken in the *xy*-plane (at z = 0) under (b) *x*-polarization and (c) *y*-polarization. (d) Calculated wavelength-dependent near-field intensities for the perfectly assembled bowtie structure when illuminated with either *x*- or *y*-polarized light. (e) Simulated scattering efficiencies for the perfect bowtie structure obtained for each polarization direction.

time allotted for nanocrystal growth, the side length of the prisms range from 100 to 150 nm and thicknesses range from 6 to 10 nm, as seen in the scanning electron microscope (SEM) image in the inset.

Figure 1b shows a finite element method (FEM) simulation for an individual Ag triangular nanoprism with a side length of 100 nm, a thickness of 8 nm, and a 1 nm radius of curvature at each of the three prism corners. (See the Methodology section for more details.) The in-plane dipolar mode occurs at λ = 679 nm and the in-plane quadrupolar peak occurs at λ = 455 nm, in good agreement with experiment. The out-of-plane quadrupolar mode is not observed because the incident plane wave is polarized in-plane. The inset shows a color map of the near-field distribution for a single prism excited at λ = 679 nm. Compared to FEM simulations, the experimental extinction curve for the colloidal sample exhibits considerable broadening of the LSPR peaks, likely due to size and shape dispersity of the synthesized nanoprisms. Small discrepancies in LSPR wavelength can be attributed to discrepancies in the refractive index of the surrounding medium, because the as-made Ag nanoprisms are capped with a polymer and are suspended in water.

In this investigation, we use modeling to evaluate the near-field and far-field optical properties of bowtie nanoatennas fabricated by nanoprism self-assembly. To build the nanoantennas, nanoprisms are assembled into junctions that possess a tip-to-tip orientation. Figure 2a shows a scanning electron microscope (SEM) image of the resulting assembly.[8] The gap sizes produced by this self-assembly method are dictated by the length of the polymer graft, which can range from 2 to 5 nm. In

comparison, the smallest junctions demonstrated for antenna structures generated by e-beam lithography are approximately 10−15 nm wide. Because bowtie antennas are well-studied plasmonic structures, we are able to make a direct comparison between the optical properties of lithographically generated structures and structures generated by nanoprism self-assembly. We use FEM simulations to investigate the optical properties of both perfect and defective nanoprism bowties. We examine the effect of common defects observed in polymer-guided nanoprism assembly, including imperfect nanoprism shape and nanoprism misalignment. We seek to determine the biggest challenges for self-assembly techniques in the manufacturing of large-scale plasmonic films or metamaterials.

METHODOLOGY

We carried out electrodynamic simulations using a commercial finite element method software package (COMSOL Multiphysics). The majority of the simulations were run on a quad core Intel i5 3.3 Ghz processor with 16 GB of RAM. Additional simulations were run on the San Diego Super Computer Center's Triton Shared Computing Cluster (TSCC). Simulation times ranged from 30 min to 12 h depending on the size of the structure being evaluated. Refractive index data for Ag was interpolated from Johnson and Christy.[16] In all simulations, the nanoprisms are modeled in an air ($n = 1$) environment, and light propagation is taken in the z-direction (out-of-plane). A substrate was not added to ease computational costs. Although other studies have clearly indicated that metal nanostructures in direct contact with a dielectric substrate experience substrate effects,[17] we do not account for such effects because the self-assembly process utilizes nanoprisms that are distributed in an isotropic polymer medium and no significant substrate effects are exhibited.

Simulations were performed for incident light with wavelengths between 430 and 1000 nm and electric field strengths of 1 V/m at standard temperature and pressure. Initial simulations were run with a step size of approximately 6 nm; to achieve better spectral resolution near the LSPR wavelength, additional simulations were run with a step size of 2 nm. The initial electric field before the addition of light was set at 0 V/m. A spherical perfectly matched layer (PML) with a radius of 1 μm and a thickness of 300 nm was used to absorb scattered waves and prevent reflective interference. Extremely fine tetrahedral meshing was used for the bowtie structure. Extremely fine meshing entails a maximum element size of 40 nm, a minimum element size of 0.4 nm, and a maximum element growth rate of 1.3. Finer tetrahedral mesh was used for the air surrounding the bowtie. Finer mesh has a maximum element size of 110 nm, a minimum element size of 8 nm, and a maximum growth rate of 1.4. The mesh used for the PML was a Finer triangular mesh that was swept across the thickness of the PML. Five layers were used, resulting in a layered shell structure binding the air and bowtie structure. The scattering boundary condition was set as the outer shell of the PML in each simulation. The far-field domain was defined as the air surrounding the bowtie, while the far-field calculation was carried out at the inner shell of the PML.

The electric field enhancement ($|E|/|E_o|$) for LSPRs corresponding to gap modes was calculated by finding the maximum electric field at the midpoint of each bowtie nanojunctions for each frequency point. For misaligned bowtie structures composed of nanoprisms rotated about the gap axis, the maximum electric field was evaluated along the gap axis (defined in Figure 6a). The field enhancement for nongap modes (evaluated for single nanoprisms, trimers, and tetramers) were calculated by finding the maximum electric field at a point 2.5 nm away from the nanoprism vertex.

The scattering efficiency is a unitless term, which is defined as the scattering cross-section (units of area) divided by the geometric cross-section (units of area).[19] To calculate the scattering efficiency, we first used the COMSOL "far-field calculation" node to calculate the far electromagnetic field, E_{far}. The geometric cross-section (CS_g) was calculated by taking the surface integral over the top surface of the Ag bowtie structure, upon which light directly impinges:

$$CS_g = \int dA \tag{1}$$

Scattering efficiencies were calculated by integrating the square of the far-field over all space and multiplying by a system-dependent constant:[18]

$$Q_{Scat} = \frac{1}{CS_g \cdot {E_o}^2} \cdot \frac{1}{{R_{PML}}^2} \cdot \int {E_{far}}^2 \cdot {R_{PML}}^2 d\Omega \tag{2}$$

where CS_g is the geometric cross-section of the bowtie and E_o is the incident electric field strength. R_{PML} is the inner radius of the PML and remains constant at 700 nm for all simulations. The R_{PML} in the integrand is added automatically by COMSOL as part of its normalization procedures, so we divide by ${R_{PML}}^2$ to remove this normalization term. In both the electric field enhancement and the scattering efficiency plots, individual data points were fitted using OriginLab's spline function for visual clarity.

Perfect Bowties. Perfect bowtie structures were modeled as two 100 nm triangular nanoprisms with an 8 nm thickness. A 1 nm radius of curvature was added to each of the three vertices. Bowties were modeled with a gap size (metal-to-metal distance) of 5 nm. The bowtie structure was placed with the dimer axis along the y-axis of the model coordinate system. The middle of the gap was placed at the coordinate origin (0,0,0), such that the bowtie structure is bisected by the xy-plane and that the xy-plane runs parallel to the basal planes of the nanoprisms. Modeling for both x- and y-polarization was done with light propagating in the z-direction.

Gap Distance. Perfect bowtie structures described above were modeled with varying gap distances of 2.5, 5, 10, 20, 40, and 80 nm. Illumination by y-polarized light was exclusively used.

Nanoprism Thickness. Perfect bowtie structures were modeled with varying nanoprism thicknesses of 8, 12, 16, and 20 nm. Illumination by y-polarized light was used exclusively. For our calculation of scattering efficiencies, it is important to note that even though the volume of the nanoprisms changes, the overall geometric cross-section (CS_g) used in the calculation remained constant. The location of the middle of the gap is kept at (0,0,0) for each simulation.

Rounded Corners. Perfect bowties with a gap size of 5 nm and a thickness of 8 nm were modeled with varying nanoprism curvatures. The radius of curvature, r, for each vertex of the nanoprisms was increased until a disk was obtained at $r = 29$ nm. Curvatures of 1, 10, and 20 nm were also modeled. Illumination by y-polarized light was used exclusively. For our calculation of scattering efficiencies, the geometric cross-section of each bowtie changed significantly with curvature, ranging from 8640 nm^2 for $r = 1$ to 5240 nm^2 for $r = 29$ nm.

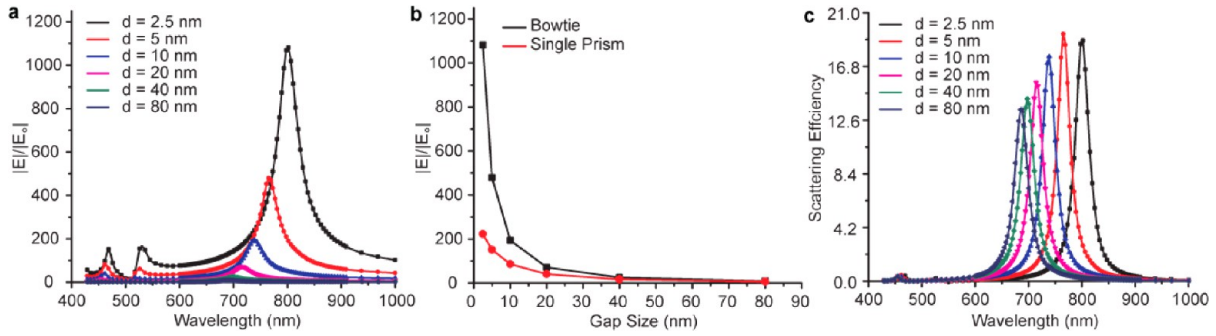

Figure 3. (a) Simulated spectra of the changes in $|E|/|E_o|$ as the gap distance of the bowtie structure increases. (b) A plot of the calculated $|E|/|E_o|$ at the midgap point versus the bowtie gap distance. Also plotted for comparison is the calculated $|E|/|E_o|$ for a single triangular nanoprism at the equivalent distance away from the prism vertex. (c) Scattering efficiencies of the bowties with respect to increasing gap distance.

Misalignment. For misaligned bowtie structures, both prisms in the bowtie were rotated with respect to the perfect bowtie axis (*y*-axis). Rotation angles of 90°−30° were modeled, where a 90° rotation defines a perfect bowtie structure. The gap distance at the closest point between the prisms was held constant at 5 nm. Illumination by *y*-polarized light was used exclusively. For misaligned bowties, both prisms comprising the dimer were rotated around the inner vertex of the bowtie structure. For this reason, the center of the bowtie gap is not at (0,0,0) but is instead shifted along the *x*-axis. Electric field enhancement was calculated as the maximum field along a line that bisects bowtie gap. To calculate the field enhancement for LSPR modes not localized to the bowtie gap, we determined the maximum electric field at a distance of 2.5 from the outer vertexes of the nanoprisms.

Trimers and Tetramers. To construct a nanoprism trimer, a third nanoprism was added to the perfect bowtie structure. The third prism was orientated so that it formed an additional perfect bowtie junction rotated at 30 degrees off of the *y*-axis with a gap distance of 5 nm. Simulations using *x*- and *y*-polarizations were performed. The electric field enhancement was calculated at both the original bowtie gap center (0,0,0), the second gap midpoint, and at each remaining vertex to compare the nongap LSPR modes. The tetramer structures were constructed with a fourth prism added to the trimer structure, forming a third perfect bowtie junction. In this structure, two of the perfect bowties are parallel to each other. In addition to the outer vertexes, the electric field enhancement was also calculated at each gap midpoint.

RESULTS AND DISCUSSION

First, we examined perfect bowtie structures generated by a nanoprism dimer where two nanoprisms are arranged in a tip-to-tip geometry and separated by a distance of 5 nm. Figure 2b,c shows cross sections of the nanoprism bowtie structure taken in the *xy*-plane at the resonant LSPR wavelengths. Figure 2d,e plots the calculated near-field enhancements and the scattering efficiencies for a perfect bowtie with respect to wavelength. For *x*-polarized light, the peak located at λ = 676 nm corresponds to excitation of a dipolar LSPR mode where light is localized to the four equivalent outer vertexes of the bowtie structure, with $|E|/|E_o|$ = 95 at a distance of 2.5 nm from each corner. For *y*-polarization, our simulations show hot spot generation within the 5 nm air gap between nanoprisms. The high degree of light localization in the bowtie gap indicates that this is the main dipolar LSPR mode for the bowtie structure, consistent with LSPR coupling between the closely spaced nanoprisms. This gap mode exhibits a field enhancement of $|E|/|E_o|$ = 479 and a large far-field scattering efficiency of Q_{scat} = 19. The spectrum in Figure 2d shows two additional peaks at 462 and 526 nm, corresponding to higher order LSPR modes where the electric near-field is localized to both the gap and to the edges or outer corners of the nanoprisms, respectively. The field enhancement associated with these higher order LSPR modes is significantly smaller than the dipolar gap mode, with $|E|/|E_o|$ = 80 and 61, respectively. These LSPR assignments are consistent with previous modeling efforts for bowtie antenna.[20]

In our self-assembly method, the gap distance between nanoprisms is determined by the length of polymer chains that are grafted to the nanoprism surface, which can be between 2 and 5 nm long. In contrast, lithographic bowtie structures tend to possess gap distances between 5 and 50 nm. To investigate how this affects light localization within the nanoprism gap, we modeled perfect bowtie structures with varying gap distances of 2.5, 5, 10, 20, 40, and 80 nm. All simulation parameters were kept the same as the previous simulation, with incident light polarized along the dimer axis. Figure 3a shows a plot of the calculated near-field intensities for each gap size, and Figure 3b shows a plot of the highest $|E|/|E_o|$ for each gap size. We observe two effects: (i) near-field enhancement increases as the gap distance decreases, and (ii) the resonant wavelength of the gap mode red-shifts as the gap distance decreases. Both observations are consistent with previous descriptions of nanoprism dimers generated by lithography.[21] For a gap distance of 2.5 nm, the LSPR peak exhibits a total redshift of $\Delta\lambda$ = 123 nm when compared to the LSPR wavelength for an isolated triangular nanoprism. Spectral peaks attributed to the excitation of higher order LSPR modes do not shift significantly with changing gap size. Figure 3b shows that $|E|/|E_o|$ in the bowtie gap decreases exponentially with increasing gap size. Here, strong plasmonic coupling occurs between the two triangular nanoprisms at gap distances <20 nm, at which point the bowtie structure is able to produce more intense hot spots than an isolated triangular nanoprism. For a gap size of 2.5 nm, the calculated field enhancement is $|E|/|E_o|$ = 1081. For gap sizes >20 nm, the maximum $|E|/|E_o|$ within the bowtie gap approaches the field enhancement obtained for a single triangular nanoprism, indicating a loss of coupling. In general, strong scattering efficiencies are only exhibited for gap distances <40 nm. Figure 3c shows the decrease in scattering efficiencies for increasing gap distances. One exception is for scattering efficiency of the bowtie possessing a 2.5 nm gap, where Q_{scat} is 0.5 units less than the scattering efficiency of a bowtie with a 5 nm gap.

dx.doi.org/10.1021/am4057612 | ACS Appl. Mater. Interfaces 2014, 6, 4134−4142

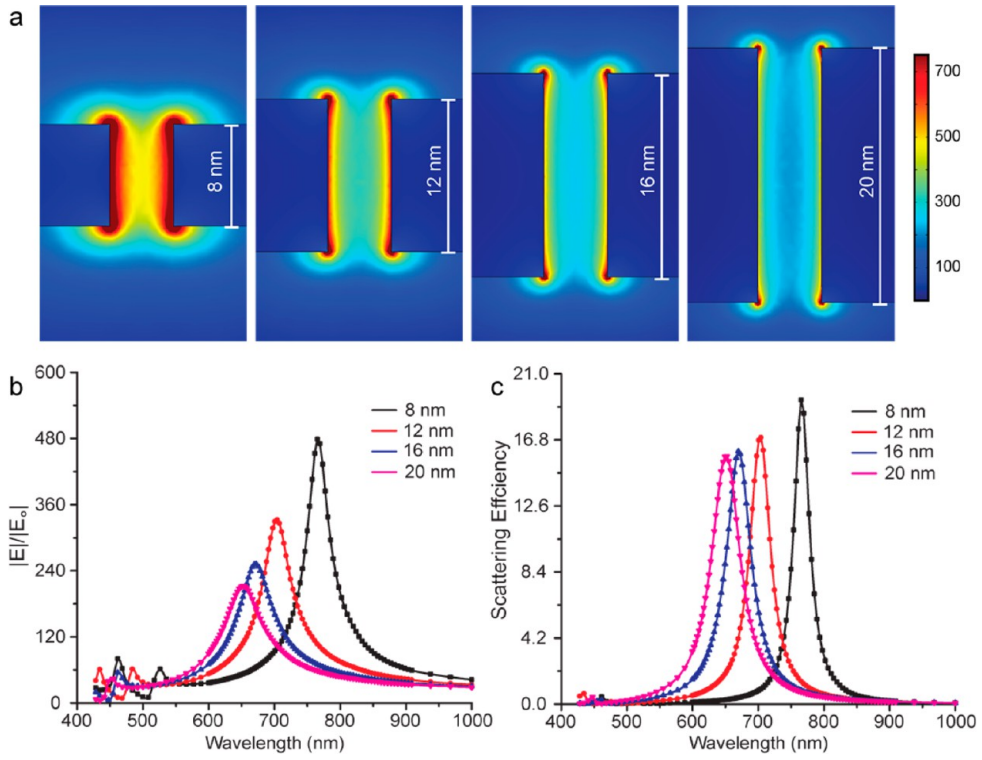

Figure 4. (a) Color maps of the near-field intensities in the *yz*-plane as the thickness of the nanoprisms comprising the assembled bowtie structure in increased. (b) The calculated $|E|/|E_o|$ and (c) corresponding far-field scattering efficiency spectra for the bowtie structure as the thickness of the nanoprism is increased from the measured nanoprism thickness of 8 to 20 nm, a typical value for structures templated by photolithography.

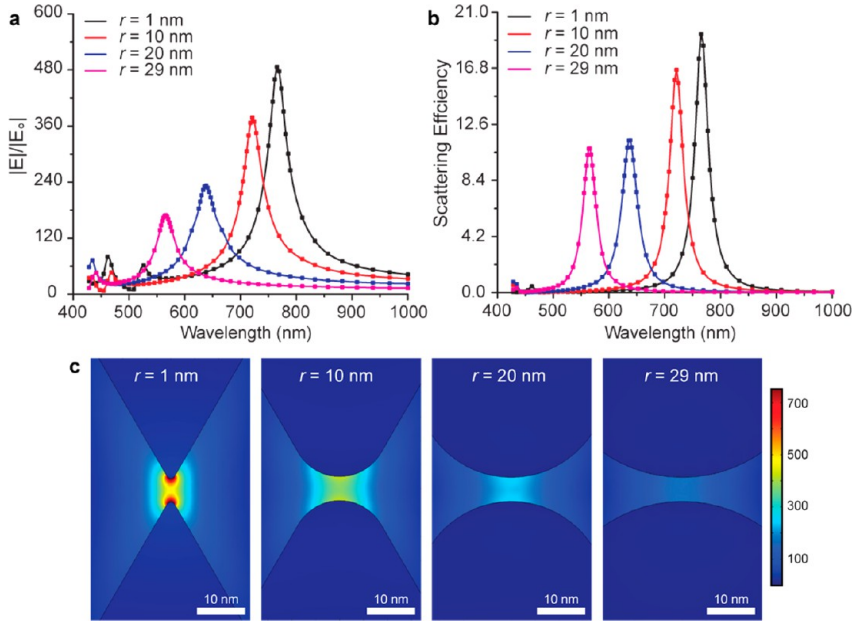

Figure 5. (a) Calculated spectra of $|E|/|E_o|$ and (b) corresponding far-field scattering efficiencies for the Ag nanoprism-based bowtie antennae as the radii of curvature of the nanoprism vertexes are increased. (c) Confinement of the electric field in the *xy*-plane each with increasing radius of curvature.

One potential challenge in utilizing colloidal triangular nanoprisms as building blocks for the self-assembly of bowtie antenna structures is the nanoprism thickness. Although nanoprism edge length can be tuned by modulating synthetic parameters such as reaction time and reactant concentration,[22,15] the overall thickness of the triangular nanoprisms is difficult to control. Typically, Ag triangular prisms are formed with a thickness of approximately 8 nm, well below the typical metal thickness obtained for top-down fabricated bowtie structures. To evaluate how nanoprism thickness affects the near-field confinement properties of the bowtie antenna, we evaluated perfect bowties with varying nanoprism thicknesses ranging from 8 nm (a typical value measured for colloidal nanoprisms) to 20 nm (in the range of bowtie thicknesses

dx.doi.org/10.1021/am4057612 | ACS Appl. Mater. Interfaces 2014, 6, 4134−4142

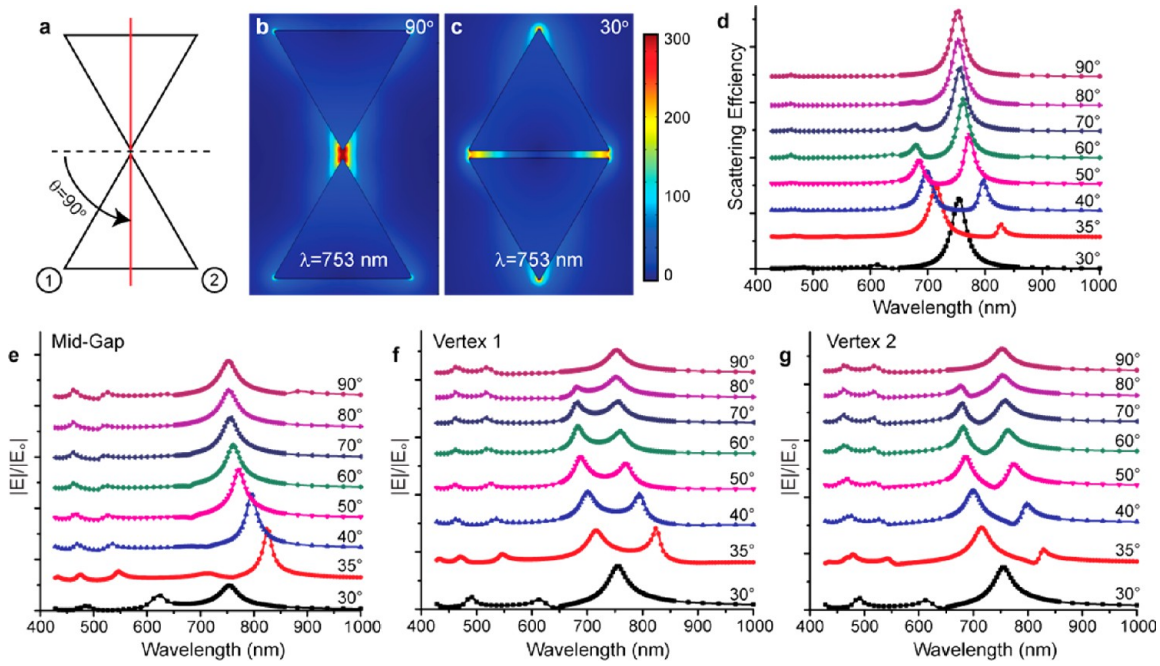

Figure 6. (a) Schematic showing how rotation of misaligned bowtie structures is determined by taking the angle θ between the gap bisector and the nanoprism bisector. A perfect bowtie structure corresponds to $\theta = 90°$. (b,c) Color maps of the near-field intensities in the *xy*-plane of bowtie structures corresponding to (b) the perfect bowtie dimer with $\theta = 90°$, and (c) the misaligned structure with $\theta = 30°$. (e–g) Calculated wavelength-dependent and angle-dependent near-field intensities for misaligned bowtie antenna at three different points located 2.5 nm away from the Ag surface: (e) in the middle of the bowite gap, (f) at Vertex 1 or the inner vertex of the misaligned bowtie, and (g) at Vertex 2 or the outer vertex of the misaligned bowtie.

obtained by electron-beam lithography). Figure 4a shows color maps of the calculated near-field intensities for the dipolar gap mode of a bowtie composed of nanoprisms with thicknesses of 8, 12, 16, and 20 nm. The images show cross sections taken in the *yz*-plane. Figure 4b,c shows plots of the near-field enhancements and scattering efficiencies of the bowtie structures. As the thickness of the Ag nanoprism increases, $|E|/|E_o|$ in the gap decreases significantly and the LSPR wavelength of gap mode blue-shifts. The thinnest bowtie structure (8 nm) exhibited the highest near-field enhancement with $|E|/|E_o| = 479$ at $\lambda = 765$ nm. Increasing the bowtie thickness to 12 nm causes this value to fall to 70% of its value, with $|E|/|E_o| = 332$ at $\lambda = 704$ nm. The thickest bowtie antennae we investigated (20 nm) resulted in a field enhancement of $|E|/|E_o| = 212$ at $\lambda = 652$ nm. This decrease in $|E|/|E_o|$ occurs because the overall illuminated surface area of the bowtie structure remains the same regardless of nanoprism thickness. Thus, any confined light within the gap is distributed over a gap volume that scales with both gap distance and nanoprism thickness. Thickness also has a minimal effect on the far-field scattering efficiency of the bowtie structures, as seen in Figure 4c.

One of the most common defects observed for nanoprism colloids is rounding and truncation of the prism corners. The Ag surfaces of prism corners possess a high surface energy due to undercoordinated surface atoms and nanoprisms often undergo aging or ripening processes where this rounding becomes more pronounced. In severe cases, rounding results in the formation of Ag disks. To investigate how these rounding defects affect the light confining ability of the bowtie antenna, we carried out simulations for bowtie structures composed of nanoprisms that possess corners with varying radii of curvature. We varied the radius of curvature from a minimum of $r = 1$ nm, representing nanoprisms with sharp triangular corners, to a maximum of $r = 29$ nm, at which point the prisms lose their in-plane anisotropy and become circular disks. Figure 5a,b plots the near-field strength and scattering efficiency of each rounded bowtie structure, and Figure 5c shows a color map of the corresponding near-field enhancements. These maps are cross sections that are taken in the *xy*-plane. As the radius of curvature increases, the near-field enhancement associated with the bowtie gap mode decreases and the dipolar gap mode exhibits a blueshift in LSPR wavelength by over 200 nm. Although the scattering efficiencies display only a 44% change for complete rounding of the nanoprism corners, the drop in near-field strength is almost an order of magnitude difference.

Next, we examine the effects of misalignment on the efficacy of bowtie antennas. In our self-assembly strategy, triangular nanoprisms assemble with a wide range of angles that are off the axis of a perfect tip-to-tip nanoprism dimer. Here, we define the structure of the bowtie by the angle of rotation between the bisecting line of the bowtie gap (along the $x = 0$ line in Figure 6a) and the bisector of the nanoprism (along the $y = 0$ line in Figure 6a). In a perfect bowtie dimer, the nanoprisms are rotated at 90° angles with respect to the gap axis. (Figure 6b) At the other extreme, the nanoprisms can adopt a perfectly misaligned structure where the nanoprisms are rotated 30° with respect to the gap in an edge-to-edge arrangement (Figure 6c). To investigate the effects of such misalignment, we modeled nanoprism dimers that adopt various angle of rotation between 30° and 90°. Figure 6d shows plots of the far-field scattering efficiencies for each off-axis bowtie structure. As the nanoprisms are rotated off the dimer axis from a perfect bowtie structure at 90° to an edge-to-edge structure at 30°, the resonant LSPR wavelength of the dipolar gap mode red-shifts from $\lambda = 765$ to $\lambda = 893$ nm and decreases in intensity. Simultaneously, a

dx.doi.org/10.1021/am4057612 | ACS Appl. Mater. Interfaces 2014, 6, 4134–4142

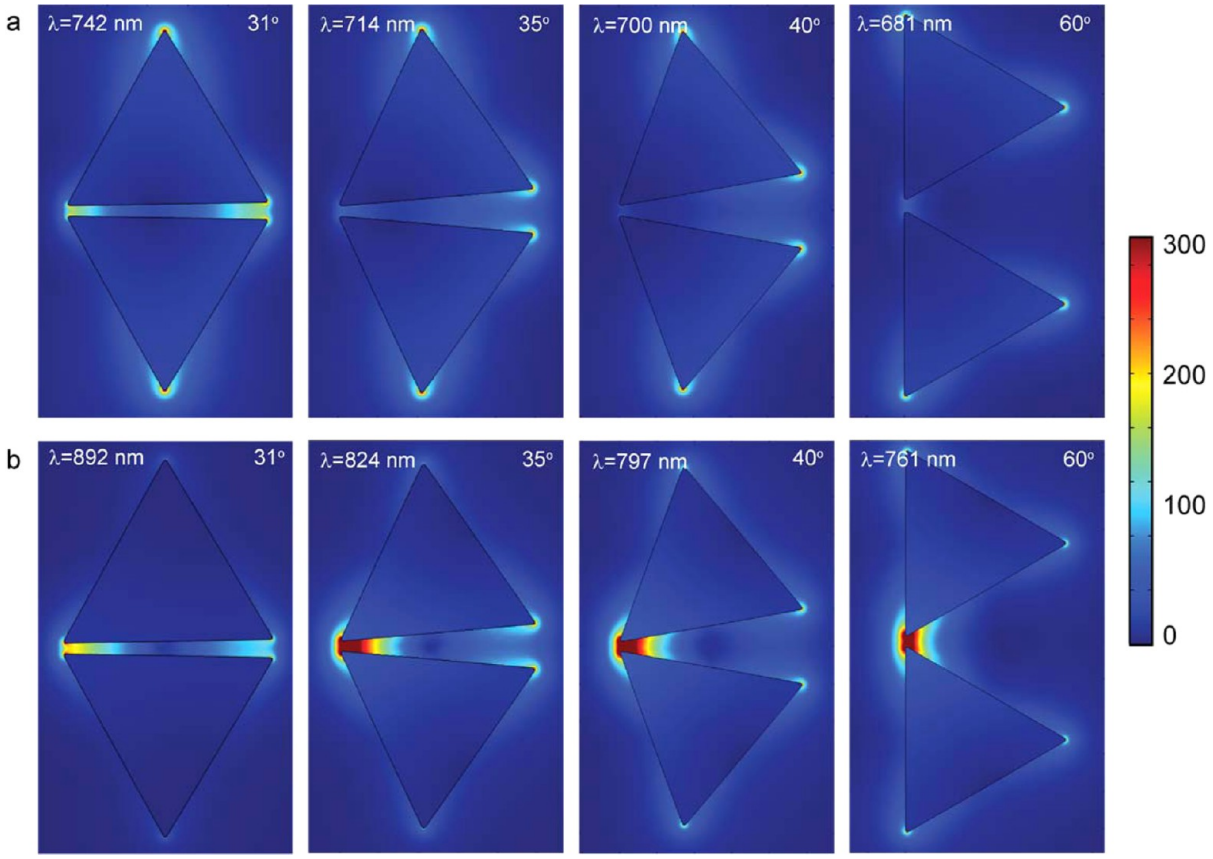

Figure 7. Color maps of the calculated near-field intensities for misaligned bowtie antenna. All images are taken as the cross-section of the bowtie structure with the *xy*-plane. The color maps show the near-field intensities for (a) the higher order resonance generated by prism rotation, and (b) the fundamental gap mode of the bowtie structure at selected angles of rotation.

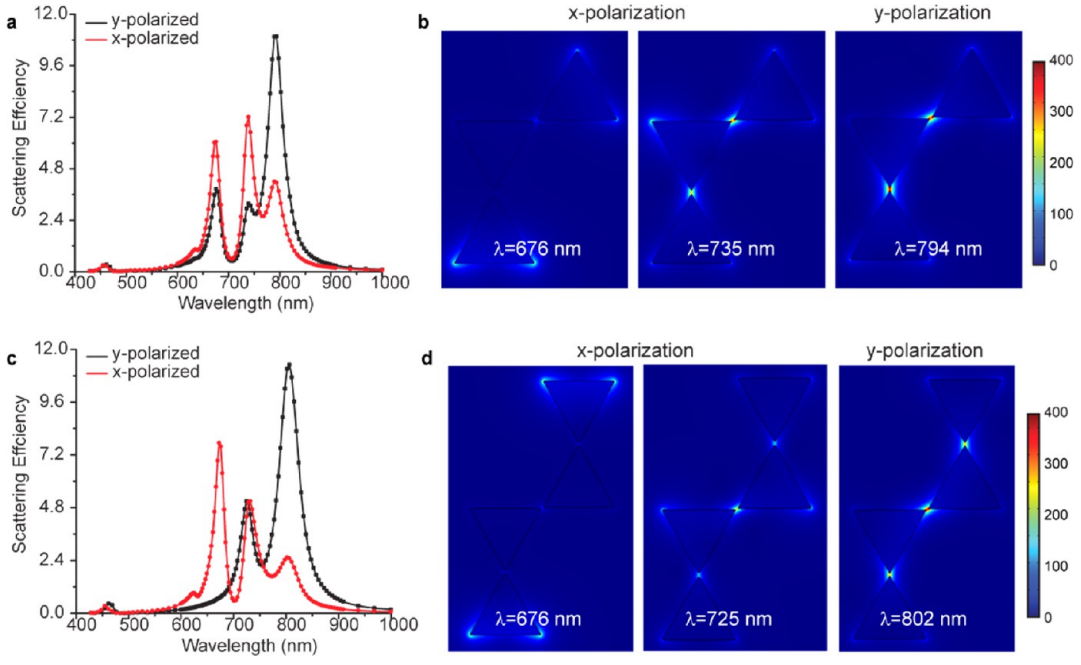

Figure 8. (a) Calculated far-field scattering efficiency spectra for a nanoprism trimer composed of three nanoprisms oriented into $\theta = 90°$ bowtie junctions under illumination with both *x*- and *y*-polarized light. (b) Color maps of the calculated near-field intensities for the trimer at the strongest resonances, as indicated by the spectral peaks in panel a. (c) Calculated far-field scattering efficiency spectra for a nanoprism tetramer composed of four nanoprisms oriented into $\theta = 90°$ bowtie junctions under illumination with both *x*- and *y*-polarized light. (d) Color maps of the calculated near-field intensities for the tetramer at the strongest resonances indicated by the spectral peaks in panel c.

dx.doi.org/10.1021/am4057612 | ACS Appl. Mater. Interfaces 2014, 6, 4134−4142

second spectral peak appears at a shorter wavelength; for the 70° bowtie structure, this peak appears at λ = 679 nm. As the rotation angle decreases toward 30°, this second peak red-shifts to λ = 714 nm and increases in intensity. Finally, upon perfect misalignment at 30°, the bowtie spectrum exhibits only a single dipolar mode with a peak of λ = 754 nm. This comes from light confinement along the slot generated by the two parallel nanoprisms facets. (Figure 6c) In this edge-to-edge arrangement, near-field intensity is not localized in the center of the gap, but rather, at the two outer ends of the gap. Figure 6e−g shows the wavelength-dependent near-field enhancements at three different locations in the nanoprism bowtie structure: in the center of the gap, at the inner vertex of a misaligned bowtie (designated Vertex 1), and at the outer vertex of a misaligned bowtie (designated Vertex 2).

Figure 7 shows the color maps of the near-fields for misaligned nanoprisms with angles of rotation between 31° and 60° for the two major spectral peaks that appear in Figure 6. These maps show that the two peaks correspond to LSPRs associated with different corners of the bowtie structure. The lower wavelength resonance red-shifts from 681 to 742 nm with increasing misalignment from 60° to 31° and corresponds to a dipolar LSPR mode associated with hot spot formation at the outer corners of the bowtie structure. In a perfect bowtie structure, this mode is only excited with *x*-polarized light and misalignment of the nanoprisms causes this mode to appear when the bowties are excited with *y*-polarized light. The higher wavelength resonance blue-shifts from 765 to 892 nm with increasing misalignment and corresponds to the fundamental gap mode of the bowtie structure. The electric field localization for this mode remains considerably high ($|E|/|E_o|$ = 626) even when the bowties are rotated at 35°. On the basis of the scattering spectra in Figure 6d, we expect that the far-field scattering response of self-assembled nanoprisms displaying a large number of these rotational defects with large angle dispersions will display a broad peak in the 700−800 nm range.

Another assembly defect commonly observed in our polymer-directed assembly method is the formation of trimer and tetramer species. We modeled the effect of these additional nanoprisms on the electric field enhancement and resonant LSPR wavelengths of the nanojunctions associated with these nanoprism clusters. Figure 8a shows the near-field enhancement spectra for the trimer structure, which is modeled as three nanoprisms arranged at perfect 90°-angle bowtie junctions. Three major spectral peaks appear, excluding the higher order modes present in the 400−550 nm range. These peaks appear at 676, 735, and 794 nm for both *x*- and *y*-polarization. Figure 8b shows the corresponding color plots of the near-field intensities associated with the trimer, from which it is apparent that the dominant peak at λ = 794 nm peak corresponds to a dipolar gap mode where light localization occurs in both junctions of the trimer. The off-center axis of the third nanoprism allows the excitation of this mode with both *x*- and *y*-polarized light, where $|E|/|E_o|$ = 210 for *x*-polarization and $|E|/|E_o|$ = 331 for *y*-polarization. This LSPR mode is red-shifted by approximately 29 nm from the major dipolar LSPR peak associated with the perfect bowtie dimer.

The tetramer structure (Figure 8c,d) exhibits major spectral peaks at 676, 725, and 802 nm. The color plots in Figure 8d show the near-field localization for LSPR excitation at these wavelengths, which indicate the excitation similar of symmetric LSPR modes as the trimer. Specifically, the peak at λ = 802 nm corresponds to a dipolar mode where light localization occurs in all three junctions of the tetramer. Analysis of the near-field enhancement at different vertexes along both the trimer and tetramer structures show that the minor spectral peaks are more difficult to deconvolute than for bowtie dimers, and stem from field localization at multiple locations along each oligomer structure. However, these simulations indicate excitation of LPSR modes where light confinement occurs between nanoprism junctions should occur in a relatively narrow wavelength region (790−805 nm) for small clusters composed of three or four nanoprisms.

CONCLUSION

We carried out electromagnetic simulations for Ag bowtie structures that are composed of self-assembled triangular nanoprisms synthesized by colloidal methods. Our simulations suggest that the small gap sizes (<5 nm) provided by self-assembly methods and the ability to fabricate bowtie structures that are extremely thin (∼8 nm) are advantageous to the construction of intense electromagnetic hot spots. We examine common defects observed in these self-assembled structures, including rounded nanoprism corners, rotational misalignment and trimer/tetramer formation. On the basis of this data, we expect that the far-field optical scattering response for self-assembled nanoprisms will display broad peaks in the 600−800 nm range due to structural heterogeneities presented by these defects. This may present difficulties for the use of self-assembly in applications where light reflection or transmission are important. However, the near-field response for both perfect and defective bowtie structures built from Ag nanoprisms is consistent, with the formation of an intense hot spot with $|E|/|E_o|$ > 200 at the midpoint between adjacent nanoprisms. The only cases for which this does not occur are bowties formed with defective nanoprisms that possess round, blunt vertexes. This suggests that for self-assembly to be a viable technique for manufacturing bowtie nanoantenna structures, appropriate surface passivation strategies must be developed to prevent shape degradation and promote long-term surface stability. One area that we did not explicitly model in this study is the effect long-range alignment and orientation over multiple bowtie structures. Our results indicate that the polarization direction of incident light relative to the bowtie axis plays a critical role in near-field enhancement associated with the self-assembled structures. Future simulation work probing the relative orientations of multiple bowtie structures may be useful in evaluating the utility of self-assembled nanoprisms for applications where large arrays of bowtie antennae are desired.

AUTHOR INFORMATION

Corresponding Author

*A. R. Tao. E-mail: atao@ucsd.edu. Phone: (858) 822-4237. Fax: (858) 534-9533.

Notes

The authors declare no competing financial interest.

ACKNOWLEDGMENTS

This work was supported through a grant from the Office of Naval Research (Award No. N000141210574), and a grant from the National Science Foundation (CMMI, Award No. 1200850).

REFERENCES

(1) Kim, S.; Jin, J.; Kim, Y.-J.; Park, I.-Y.; Kim, Y.; Kim, S.-W. High-harmonic generation by resonant plasmon field enhancement. *Nature* **2008**, *453* (7196), 757−760.

(2) Lesuffleur, A.; Kumar, L. K. S.; Gordon, R. Enhanced second harmonic generation from nanoscale double-hole arrays in a gold film. *Appl. Phys. Lett.* **2006**, *88* (26), 261104−1−3.

(3) van Nieuwstadt, J. A. H.; Sandtke, M.; Harmsen, R. H.; Segerink, F. B.; Prangsma, J. C.; Enoch, S.; Kuipers, L. Strong Modification of the Nonlinear Optical Response of Metallic Subwavelength Hole Arrays. *Phys. Rev. Lett.* **2006**, *97* (14), 146102−1−4.

(4) Haynes, C. L.; Van Duyne, R. P. Nanosphere Lithography: A Versatile Nanofabrication Tool for Studies of Size-Dependent Nanoparticle Optics. *J. Phys. Chem. B* **2001**, *105* (24), 5599−5611.

(5) Jensen, T. R.; Malinsky, M. D.; Haynes, C. L.; Van Duyne, R. P. Nanosphere Lithography: Tunable Localized Surface Plasmon Resonance Spectra of Silver Nanoparticles. *J. Phys. Chem. B* **2000**, *104* (45), 10549−10556.

(6) Ross, B. M.; Lee, L. P. Plasmon tuning and local field enhancement maximization of the nanocrescent. *Nanotechnology* **2008**, *19* (27), 275201.

(7) Bukasov, R.; Shumaker-Parry, J. S. Highly Tunable Infrared Extinction Properties of Gold Nanocrescents. *Nano Lett.* **2007**, *7* (5), 1113−1118.

(8) Gao, B.; Alvi, Y.; Rosen, D.; Lav, M.; Tao, A. R. Designer nanojunctions: orienting shaped nanoparticles within polymer thin-film nanocomposites. *Chem. Commun.* **2013**, *49* (39), 4382−4384.

(9) Gao, B.; Arya, G.; Tao, A. R. Self-orienting nanocubes for the assembly of plasmonic nanojunctions. *Nat. Nanotechnol.* **2012**, *7* (7), 433−437.

(10) Guo, H.; Meyrath, T. P.; Zentgraf, T.; Liu, N.; Fu, L.; Schweizer, H.; Giessen, H. Optical resonances of bowtie slot antennas and their geometry and material dependence. *Opt. Express* **2008**, *16* (11), 7756−7766.

(11) Hatab, N. A.; Hsueh, C.-H.; Gaddis, A. L.; Retterer, S. T.; Li, J.-H.; Eres, G.; Zhang, Z.; Gu, B. Free-Standing Optical Gold Bowtie Nanoantenna with Variable Gap Size for Enhanced Raman Spectroscopy. *Nano Lett.* **2010**, *10* (12), 4952−4955.

(12) Sundaramurthy, A.; Schuck, P. J.; Conley, N. R.; Fromm, D. P.; Kino, G. S.; Moerner, W. E. Toward Nanometer-Scale Optical Photolithography: Utilizing the Near-Field of Bowtie Optical Nanoantennas. *Nano Lett.* **2006**, *6* (3), 355−360.

(13) Yu, N.; Cubukcu, E.; Diehl, L.; Bour, D.; Corzine, S.; Zhu, J.; Höfler, G.; Crozier, K. B.; Capasso, F. Bowtie plasmonic quantum cascade laser antenna. *Opt. Express* **2007**, *15* (20), 13272−13281.

(14) Kinkhabwala, A.; Yu, Z.; Fan, S.; Avlasevich, Y.; Mullen, K.; Moerner, W. E. Large single-molecule fluorescence enhancements produced by a bowtie nanoantenna. *Nat. Photonics* **2009**, *3* (11), 654−657.

(15) Jin, R.; Cao, Y.; Mirkin, C. A.; Kelly, K. L.; Schatz, G. C.; Zheng, J. G. Photoinduced Conversion of Silver Nanospheres to Nanoprisms. *Science* **2001**, *294* (5548), 1901−1903.

(16) Johnson, P. B.; Christy, R. W. Optical Constants of the Noble Metals. *Phys. Rev. B: Condens. Matter Mater. Phys.* **1972**, *6* (12), 4370−4379.

(17) Jiao, X.; Goeckeritz, J.; Blair, S.; Oldham, M. Localization of Near-Field Resonances in Bowtie Antennae: Influence of Adhesion Layers. *Plasmonics* **2009**, *4* (1), 37−50.

(18) Knight, M. W.; Halas, N. J. Nanoshells to nanoeggs to nanocups: optical properties of reduced symmetry core−shell nanoparticles beyond the quasistatic limit. *New J. Phys.* **2008**, *10* (10), 105006.

(19) Bohren, C. F.; Huffman, D. R. Absorption and Scattering by an Arbitrary Particle. In *Absorption and Scattering of Light by Small Particles*; Wiley-VCH Verlag GmbH: Weinheim, Germany, 1998; pp 71−72.

(20) Ding, W.; Bachelot, R.; Kostcheev, S.; Royer, P.; Espiau de Lamaestre, R. Surface plasmon resonances in silver Bowtie nanoantennas with varied bow angles. *J. Appl. Phys.* **2010**, *108* (12), 124314−1−6.

(21) Fromm, D. P.; Sundaramurthy, A.; Schuck, P. J.; Kino, G.; Moerner, W. E. Gap-Dependent Optical Coupling of Single "Bowtie" Nanoantennas Resonant in the Visible. *Nano Lett.* **2004**, *4* (5), 957−961.

(22) Goebl, J.; Zhang, Q.; He, L.; Yin, Y. Monitoring the Shape Evolution of Silver Nanoplates: A Marker Study. *Angew. Chem., Int. Ed.* **2012**, *51* (2), 552−555.